

Northumbria Research Link

Citation: Shen, Xiang, Avital, Eldad, Paul, Gordon, Rezaenia, Mohammad Amin, Wen, Pihua and Korakianitis, Theodosios (2016) Experimental study of surface curvature effects on aerodynamic performance of a low Reynolds number airfoil for use in small wind turbines. *Journal of Renewable and Sustainable Energy*, 8 (5). 053303. ISSN 1941-7012

Published by: American Institute of Physics

URL: <https://doi.org/10.1063/1.4963236> <<https://doi.org/10.1063/1.4963236>>

This version was downloaded from Northumbria Research Link:
<http://nrl.northumbria.ac.uk/id/eprint/43491/>


Northumbria University has developed Northumbria Research Link (NRL) to enable users to access the University's research output. Copyright © and moral rights for items on NRL are retained by the individual author(s) and/or other copyright owners. Single copies of full items can be reproduced, displayed or performed, and given to third parties in any format or medium for personal research or study, educational, or not-for-profit purposes without prior permission or charge, provided the authors, title and full bibliographic details are given, as well as a hyperlink and/or URL to the original metadata page. The content must not be changed in any way. Full items must not be sold commercially in any format or medium without formal permission of the copyright holder. The full policy is available online: <http://nrl.northumbria.ac.uk/policies.html>

This document may differ from the final, published version of the research and has been made available online in accordance with publisher policies. To read and/or cite from the published version of the research, please visit the publisher's website (a subscription may be required.)

Experimental study of surface curvature effects on aerodynamic performance of a low Reynolds number airfoil for use in small wind turbines

Cite as: J. Renewable Sustainable Energy **8**, 053303 (2016); <https://doi.org/10.1063/1.4963236>

Submitted: 09 March 2016 . Accepted: 09 September 2016 . Published Online: 29 September 2016

Xiang Shen, Eldad Avital, Gordon Paul, Mohammad Amin Rezaenia, Pihua Wen , and Theodosios Korakianitis



View Online



Export Citation



CrossMark

ARTICLES YOU MAY BE INTERESTED IN

[Low Reynolds number airfoil optimization for wind turbine applications using genetic algorithm](#)

Journal of Renewable and Sustainable Energy **5**, 052007 (2013); <https://doi.org/10.1063/1.4822037>

[Turbulent intensity and Reynolds number effects on an airfoil at low Reynolds numbers](#)
Physics of Fluids **26**, 115107 (2014); <https://doi.org/10.1063/1.4901969>

[Effect of trailing edge shape on the separated flow characteristics around an airfoil at low Reynolds number: A numerical study](#)

Physics of Fluids **29**, 014101 (2017); <https://doi.org/10.1063/1.4973811>



NEW: TOPIC ALERTS

Explore the latest discoveries in your field of research

SIGN UP TODAY!



Experimental study of surface curvature effects on aerodynamic performance of a low Reynolds number airfoil for use in small wind turbines

Xiang Shen,^{1,2} Eldad Avital,¹ Gordon Paul,¹ Mohammad Amin Rezaenia,¹ Pihua Wen,¹ and Theodosios Korakianitis^{3,a)}

¹School of Engineering and Materials Science, Queen Mary University of London, Mile End Road, London E1 4NS, United Kingdom

²Tianjin Jinhang Computing Technology Research Institute, Tianjin 300308, China

³Parks College of Engineering, Aviation and Technology, Saint Louis University, St. Louis, Missouri 63103, USA

(Received 9 March 2016; accepted 9 September 2016; published online 29 September 2016)

This paper presents the wind tunnel experimental results to investigate the effects of surface gradient-of-curvature on aerodynamic performance of a low Reynolds number airfoil Eppler 387 for use in small-scale wind turbines. The prescribed surface curvature distribution blade design method is applied to the airfoil E387 to remove the gradient-of-curvature discontinuities and the redesigned airfoil is denoted as A7. Both airfoils are manufactured with high precision to reflect the design. Low-speed wind tunnel experiments are conducted to both airfoils at chord based Reynolds numbers 100 000, 200 000, and 300 000. Surface pressure measurements are used to calculate the lift and pitching-moment data, and the wake survey method is applied to obtain the drag data. The experimental results of E387 are compared with NASA Low Turbulence Pressure Tunnel (LTPT) results for validation. The gradient-of-curvature discontinuities of E387 result in a larger laminar separation bubble which causes higher drag at lower angles of attack. As the angle of attack increases the separation bubble of the airfoil E387 moves faster towards the leading edge than that of A7, resulting in a premature bubble bursting and earlier stall on E387. The impact of the gradient-of-curvature distribution on the airfoil performance is more profound at higher angles of attack and lower Reynolds number. The aerodynamic improvements are integrated over the 3D geometry of a 3 kW small wind turbine, resulting in up to 10% increase in instantaneous power and 1.6% increase in annual energy production. It is experimentally concluded that an improved curvature distribution results in a better airfoil performance, leading to higher energy output efficiency. *Published by AIP Publishing.* [<http://dx.doi.org/10.1063/1.4963236>]

I. INTRODUCTION

Small wind turbines are generally defined as wind turbines with a rated capacity up to 50 kW. They are very widely used for residential and farming purposes, and can also be used as a combination with other clean energy technologies such as hydro engines and photovoltaic. According to the report from the World Wind Energy Association (WWEA),¹ more than 806 000 small wind turbines were installed globally before 2013, and this fast growing market will bring a cumulative installed capacity of approximately 3 GW by the year 2020.

The smaller sizes and dimensions of small wind turbine blades make their chord based Reynolds numbers at different blade sections (airfoils) remarkably smaller compared to large-scale wind turbines.² Typically, Reynolds numbers for small wind turbines are on the order of 10^5 or even less while large-scale wind turbines often operate at a Reynolds number in excess of 10^6 .^{3,4}

^{a)}Electronic mail: korakianitis@alum.mit.edu

Operating at low Reynolds numbers, small wind turbines do not always offer good aerodynamic performance subjected to inherent effects of flow separation and stall on the blades. The flow on blade sections separates due to a sufficiently large magnitude of the adverse pressure gradient and changes in flow geometry including local surface curvature variations at low Reynolds numbers. The flow experiences transition to the turbulence and can result in a stall (without turbulent re-attachment) or a laminar separation bubble (LSB) (with turbulent re-attachment).⁵ Either way, the overall aerodynamic performance of the blades is reduced and hence the output power of wind turbines is decreased.⁶

The conventional airfoils used in large-scale wind turbines become inappropriate for small wind turbines due to the operating Reynolds number difference.⁷ Hence, researchers have put great efforts to develop low Reynolds airfoils for small wind turbines. Giguere and Selig⁸ presented three primary airfoils with 10% maximum thickness and one root airfoil with 16% maximum thickness (SG604X family), which are specially designed for 1–5 kW rated power small wind turbines. The wind tunnel tests confirmed that they have enhanced the lift-drag performance over many other low Reynolds number airfoils. Based on the genetic algorithm, Ram *et al.*⁹ designed a low Reynolds airfoil USPT2 with 10% maximum thickness. They claimed that the airfoil has a better lift-drag performance than the SG604X family⁸ when the attack angle is beyond 10° and the lift drop beyond the stalling angle is milder than similar airfoils. National Renewable Energy Laboratory (NREL) specifically designed airfoils S822 and S834¹⁰ for the small wind turbines and S834 took low noise into design consideration. These two airfoils were experimentally proved to have more steady stall performance at $Re = 5 \times 10^5$. Moreover, using a pressure-load prescription method, Henriques *et al.*¹¹ designed an airfoil with high lift performance (C_l is close to 2) for urban wind turbines at Reynolds numbers ranging from 6×10^4 to 10^6 . More recent researches for small wind turbine airfoil design can also be found in the study of Islam *et al.*,¹² Marnett *et al.*,¹³ and Singh *et al.*^{6,14}

Researchers have noticed that low Reynolds number airfoil performance is dominated by laminar separation bubbles. McGhee *et al.*¹⁵ conducted wind tunnel tests on the airfoil E387 over a range of low Reynolds numbers and concluded that at Reynolds numbers below 200 000 laminar separation bubbles dominate the airfoil performance. Selig *et al.*¹⁶ tested six low Reynolds airfoils for small wind turbine use and confirmed these low Reynolds number operations are highly dependent on the laminar boundary layer behaviour. Van Treuren⁷ compared the low Reynolds number airfoil performance results between wind tunnel tests and commonly used computational tools, and once again confirmed the necessity of the airfoil wind tunnel experiments at low Reynolds numbers. The separation bubble increases the boundary layer thickness above the airfoil, resulting in the loss of lift force and increase of pressure drag. Hence, the small wind turbine's power generation efficiency is degraded.

Consequently, to optimise small wind turbine efficiency by improving the airfoil performance, flow separation must be suppressed. Researchers have shown that flow separation can be suppressed by making the curvature distribution of an airfoil continuous and smooth.^{17,18} The idea originated from high-efficiency turbomachinery blade design, in which the distribution of surface curvature is an important factor.^{19,20} In 1985, a pressure spike was detected by Hodson²¹ which was caused by the curvature discontinuity at the connecting position between the leading edge (LE) circle and the airfoil main body. Consequently, great efforts were made to remove the LE spike and keep a smooth pressure distribution.^{22,23} Wheeler *et al.*^{24,25} found that the LE geometry also affects the compressor efficiency through the interaction between compressor LE and wake. Massardo *et al.*^{26,27} used the streamline curvature distribution calculations to determine the 3D variation of inlet and outlet flow angles for axial-flow compressor design and improved the compressor efficiency. Korakianitis *et al.* proposed a design method²⁸ to optimize airfoils by ensuring continuous distributions of curvature and gradient-of-curvature along the surfaces, and showed that the aerodynamic and heat transfer performance strongly depended on curvature and gradient-of-curvature distributions. Based on the surface curvature distribution, Song *et al.*²⁹ showed that continuous curvature distribution at the LE blending position of a compressor blade improves the performance by helping to eliminate the separation bubble.

Although the effects of surface curvature discontinuities are widely researched in turbomachinery blade design, more research attention is required on external aerodynamics applications considering the prospective impacts of surface curvature distribution on the behaviour of the airfoil boundary layer. Korakianitis *et al.*²⁸ applied continuous gradient-of-curvature distributions to wind turbine airfoils and numerically presented the aerodynamic improvements of the airfoils. Based on that, Shen *et al.*³⁰ separately investigated the effects of surface curvature and gradient-of-curvature on the boundary layer behaviour of different airfoils. They numerically concluded that the continuous distributions of surface curvature and gradient-of-curvature improve the aerodynamic performance through the effects on the laminar boundary layer. Nevertheless, more experimental research is needed on the aerodynamic mechanisms causing the improved airfoil performance yielded by smooth curvature distribution as the relevant research on airfoils in small wind turbines has not been investigated and published before to the best of the authors' knowledge.

In this paper, we experimentally examine the effects of improving gradient-of-curvature distributions on an external airfoil. A typical low Reynolds number airfoil E387 is selected for this investigation due to the existence of discontinuities of gradient-of-curvature, its extensive applications, and the available experimental data.^{15,16} All the gradient-of-curvature discontinuities of airfoil E387 are removed using the CIRCLE method.³¹ The newly designed airfoil is denoted as "A7." Both airfoil manufacturing and wind tunnel experiments were carried out in Queen Mary University of London (QMUL). The experiment carried out in the NASA Langley Low Turbulence Pressure Tunnel (LTPT),¹⁵ which is regarded as a benchmark of E387, is selected as the reference to validate the experimental results of the airfoil E387 from this study. The experimental results of the two airfoils are compared to analyze the aerodynamic performance differences caused by the different curvature distributions. We also examine the mechanism behind the observed changes with both experimental and computational results. Reynolds Averaged Navier-Stokes (RANS) computations are applied to both airfoils at the same operating conditions as the experiments. The experimental results are subsequently applied on a 3 kW wind turbine to estimate the power generation improvements. It is anticipated that the results in this paper will deepen our knowledge of surface curvature effects on the aerodynamic performance of low Reynolds number airfoils.

II. REDESIGN OF THE AIRFOIL E387 WITH THE CIRCLE METHOD

Many airfoil geometries including E387 have discontinuities in surface gradient-of-curvature distributions.³¹ These discontinuities are observable as unsmooth "kinks" in airfoil curvature distributions. A smooth curvature distribution is equivalent to a continuous gradient-of-curvature distribution. Based on this, the CIRCLE method, which was previously documented,³¹ is applied to the airfoil E387 to remove the discontinuities in gradient-of-curvature distributions. The original and redesigned airfoils are presented in Fig. 1. The curvature distributions are presented in Fig. 1(a) and the geometries are compared in Fig. 1(b). The curvature distributions

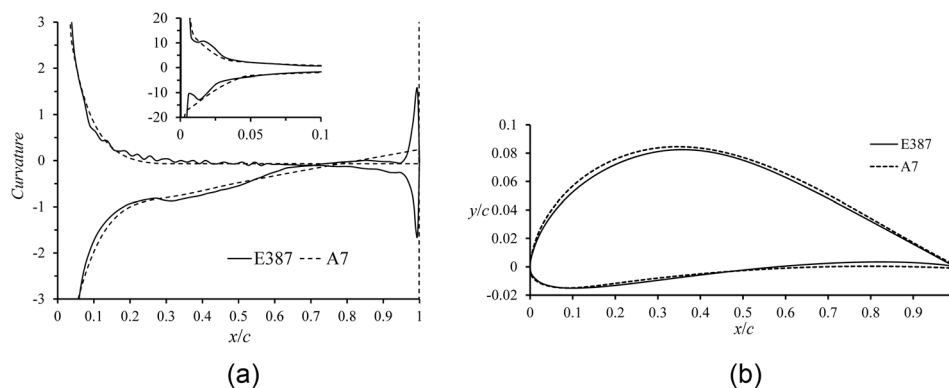


FIG. 1. The comparison of (a) curvature distributions and (b) airfoil geometries of the original aerofoil E387²⁸ and the redesigned airfoils A7. The inset in (a) is the magnification of the curvature distributions at the leading edge area.

are calculated from the definition of surface curvature, as shown in Eq. (1), and the definition of slope-of-curvature is presented in Eq. (2). The sign of the curvature is usually defined as the direction of the unit tangent vector moving along the curve. In order to clearly present the curvature distributions of both suction and pressure sides simultaneously, we define curvature as positive if the vector rotates clockwise (suction side) from the LE, otherwise it is negative (pressure side)

$$Curv = \frac{1}{r} = \frac{y''}{(1 + y'^2)^{3/2}}, \quad (1)$$

$$Curv' = \frac{d(Curv)}{dx} = \frac{y'''(1 + y'^2) - 3y'y''^2}{(1 + y'^2)^{5/2}}. \quad (2)$$

In Fig. 1(a), the unsmooth parts (gradient-of-curvature discontinuities) including two obvious “kinks” in the magnified figure are exhibited on both sides of the airfoil E387, although most of the gradient-of-curvature discontinuities are in the suction surface. The airfoil A7 has a smooth curvature distribution without any gradient-of-curvature discontinuities. The continuous gradient-of-curvature distribution of A7 results in very slight differences in thickness and camber distributions.

III. EXPERIMENTAL FACILITY AND MEASUREMENT TECHNIQUES

Wind tunnel measurements were conducted to compare the performance of the original airfoil E387 and the redesigned airfoil A7 at Reynolds numbers 100 000, 200 000, and 300 000. Static surface pressure measurements were performed to obtain pressure, lift, and pitching-moment coefficients. Wake profile measurements were performed to obtain the drag coefficients.

A. Wind tunnel facility

The experimental study was conducted in QMUL No. 2 subsonic wind tunnel. This closed-circuit type tunnel has a 5.6:1 contraction ratio. The test section is 760 mm high, 1000 mm wide, and 2330 mm long. An exchangeable section was specifically designed for the current airfoil performance testing. The wind speeds in the test section are variable up to 40 m/s controlled by an AC motor and a five bladed fan. The turbulence intensity (TI) in the testing section, which has been measured by a DANTEC 55P11 single hot wire with a Dantec 55M01 constant-temperature anemometer (CTA), is 0.4% to 0.6% depending on the Reynolds number. The low TI is sufficient for aerodynamic performance measurements for low Reynolds number airfoils. The continuous flow quality has also been tested and confirmed in the experiment.³²

Amandolese and Szechenyi³³ suggested that the stalling angle of the aerofoil does not vary significantly for the wind tunnel experiments with TI lower than 1.1%. However, higher TI in the testing section can result in delay of stall to various extents, and a more significant delay of stall can be observed with an increasing TI.^{34,35} It will be of interest to investigate the effects of TI on the aerofoil performance, yet it is beyond the scope of this article. In the present study, the attention is paid to the effects of the slope-of-curvature discontinuities on the performance of low Reynolds number aerofoils. Hence, we tested the original and redesigned aerofoils at the same operating conditions, i.e., in the same wind tunnel with a consistent TI. It is essential to first study the low TI conditions before addressing the effect of higher TI and we believe that this is the first step to conduct series of studies.

B. Airfoil models

Each airfoil model was mounted vertically in the wind tunnel. The model is comprised of three sections, the upper section, middle section, and lower section. The 200 mm middle section was machined from the aluminum alloy by a computer numerical control (CNC) machine HAAS Mini Mill with a positioning accuracy of 0.005 mm. The upper and lower sections were

3D printed using the material ABS M30 by Stratasys Fortus 450mc with an achievable accuracy of 0.127 mm. The span length of each section is 280 mm. Three studding rods penetrate all the sections and are fixed with nuts at the end of the upper section.

Three 5 mm Dowel pins are used to connect the neighboring sections. The lower section of each airfoil was fitted with a 30 cm diameter endplate which is embedded and rotatable in the bottom of the test section. One 8 mm dowel pin was used to connect the upper section and the ceiling of the test section. It is an interference fit between the dowel pin and upper section, and a sliding fit between the dowel pin and ceiling. In this way, the angle of attack (AoA) can be adjusted by rotating the scaled endplate embedded in the bottom of the test section. The pitching axis of the airfoil was located at the quarter-chord point which is a common approximate location of the aerodynamic center.

Both models have a chord length of 228.6 mm (9 in.) and a span of 760 mm. To deal with the “zero thickness” trailing edge (TE) problem and provide structural integrity, the TE of the airfoil model E387 was circularly cut to keep the TE diameter as 5 mm. The structure of the middle section is presented in Fig. 2. To keep the surface curvature of the airfoils to the maximum, all the pressure tubing was routed under the surface. It was a necessary compromise to sacrifice some space for pressure tubing near the TE (say at $x/c \geq 0.9$) to provide sufficient structure strength without damaging the surface curvature. 41 pressure measurement orifices were drilled through the metal surface of the middle part into the tubing. The axes of the orifices were perpendicular to the tangential direction of local surface. These 0.4 mm diameter orifices were slightly staggered spanwise to avoid the interference from each other.

The models were digitized using a QCT Quantum GL 6105 coordinate measuring machine (CMM) to determine the actual airfoil shape in order to determine the accuracy of the manufactured models. 256 points were taken around the airfoil. The measured spacing was proportional to the local curvature. Relatively more points were taken near the LE and TE than near the airfoil main body. All model coordinates were measured near middle of the model. The curvature distributions calculated from the measured model coordinates are presented in Fig. 3. High-precision manufacture effectively preserved the original design. The main differences between the curvatures are near LE and TE. The main body part of each airfoil keeps a smooth curvature distribution with a small value. In Fig. 3(a), the unsmooth curvature distributions of E387 at the connection part between the LE and the main body indicates that the manufactured airfoil model E387 successfully retains the gradient-of-curvature discontinuities in the original design. As designed in Sec. II, the curvature distributions of A7 in Fig. 3(b) removed the gradient-of-curvature discontinuities. The precision limit of airfoil manufacture and coordinate measurement introduced slight fluctuations to both curvature distributions. Generally, the two airfoils met the design and wind tunnel testing requirements.

C. Measurement techniques and correction methods

1. Surface pressure measurements

The surface pressure distributions were obtained from 41 pressure orifices distributed over the surface of each airfoil. Silicone tubes were used to connect the surface pressure orifices

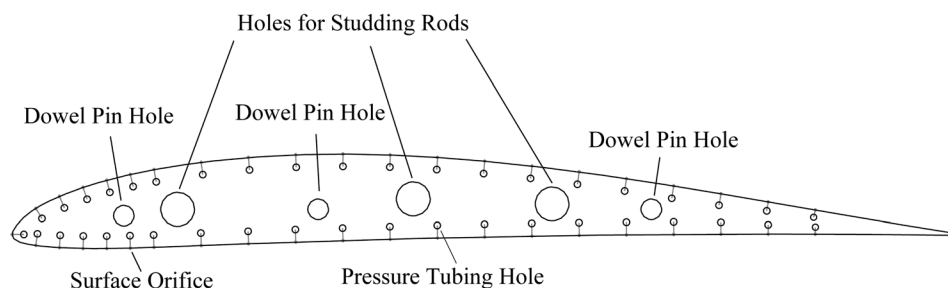


FIG. 2. The schematic figure of the inside structure of the airfoil middle section.

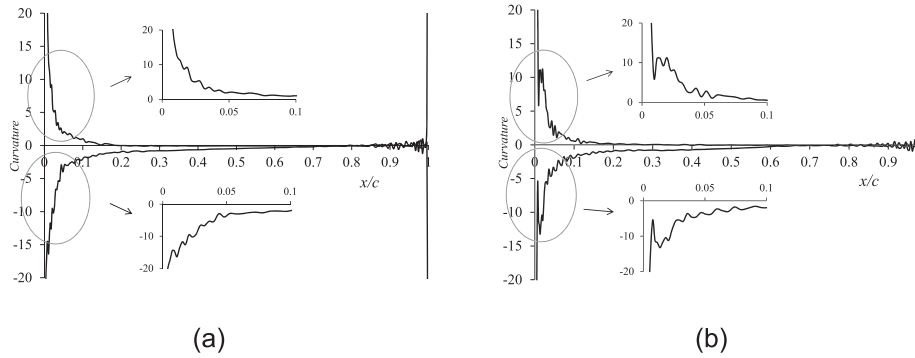


FIG. 3. Curvature distributions of the airfoils E387 (a) and A7 (b) calculated from the measured coordinates of manufactured airfoils. The smaller figures are magnifications of the curvature at the leading edge area ($0 < x/c < 0.1$).

through 1.5 mm copper inserts to the external Scanivalve DSA3217 pressure transducers. The pressure transducer output signal was sampled at 100 Hz for 10 s for each orifice. All the measured data were digitized by a NI 6040E analog-to-digital data acquisition board. The instantaneous surface pressure values were subsequently averaged to obtain the mean pressure at various orifice positions for all angles of attack from 0° to 14° . Pressure coefficients were obtained from the surface pressure measurements. The lift coefficients and pitching moment coefficients about the quarter-chord point were integrated from the pressure coefficients.

2. Wake survey

The wake measurements were performed 300 mm behind the TE of the airfoil to make sure that the wake static pressure had recovered to the normal static pressure. Three total-pressure tubes spaced 50 mm were used to take the wake profile measurements over the 100 mm center span of each model. The measured points were spaced 1 mm apart in the wake deficit zone. Depending on the width of the wake profile, every probe performed 60 to 80 total-pressure measurements in each wake survey traverse. The wake survey measurements were conducted until the appearance of the unsteadiness of the wake (approximately 11°). The flow that passes over the aerofoil suffers momentum loss and this loss is related to the profile drag per unit span d which can be described as follows:

$$d = \frac{1}{b} \iint \rho V (V_\infty - V) da, \quad (3)$$

where b is the span length, ρ is the air density, V is the wake velocity at the elemental area da in the plane that is perpendicular to the air flow, and V_∞ is freestream flow velocity. The drag coefficient C_d can be obtained correspondingly according to the definition.

3. Air density correction

Since certain Reynolds numbers rather than certain wind speeds are required in this experiment, accurate calculation of air density is extremely important besides the determination of the wind speed and the dynamic viscosity of the air according to the definition of Reynolds number.

The density of dry air is usually calculated from the ideal gas law. However, the relative humidity of the air in London is considerably high when the experiments were conducted. The addition of water vapor to air remarkably reduces the density of the air (up to 20%) and therefore is not neglected. Shelquist's correction of air humidity³⁶ is applied and the air is treated as a mixture of water vapor and dry air. The density can be expressed as

$$\rho_h = \frac{p_d}{R_d T} + \frac{p_v}{R_v T}, \quad (4)$$

where R_d and R_v are specific gas constants for dry air and water, subscripts h , d , and v , respectively, denote humid air, dry air, and water vapor. The summation of p_d and p_v is local atmospheric pressure and p_v can be expressed as

$$p_v = \phi p_s, \quad (5)$$

where ϕ is the relative humidity of the air, p_s is the saturation vapor pressure which can be expressed as a function of local temperature³⁷

$$p_s = 6.1078 \times 10^{\frac{7.5T}{T+237.3}}. \quad (6)$$

This method reduces the error in the density calculation to less than 0.2% in the temperature range of -10°C to 50°C .³⁶

4. Two-dimensional corrections

Standard low speed wall boundary corrections for two-dimensional wind tunnel testing³⁸ have been applied to the experimental data. Due to the existence of solid and wake blockage, corrections were applied to the free stream dynamic pressure. The streamline curvature corrections were applied to angle of attack, lift, and pitching moment because of the physical constraints of the tunnel boundaries,

$$\alpha' = \alpha + \frac{57.3\sigma}{2\pi} (C_l + 4C_m), \quad (7)$$

$$C_l' = C_l(1 - \sigma - 2\varepsilon), \quad (8)$$

$$C_m' = C_m(1 - 2\varepsilon) + \frac{1}{4}\sigma C_l, \quad (9)$$

where the variables with $'$ are corrected data, and blockage ε is the summation of the solid blockage ε_{sb} and wake blockage ε_{wb} . For the above, $\sigma = \frac{\pi^2}{48} \left(\frac{c}{h}\right)^2$ where c is the model chord length and h is the tunnel height. Unaffected by streamline curvature, the drag was corrected from the dynamic pressure effect and the wake blockage

$$C_d' = C_d(1 - 3\varepsilon_{sb} - 2\varepsilon_{wb}). \quad (10)$$

No blockage corrections were applied to the pressure coefficient data. For the current experiments, we applied all the pressure orifices near the center of the airfoil model with a span-to-chord ratio of 4.5 to reduce the effects of the tunnel sidewall boundary layer interference.

IV. RESULTS AND DISCUSSION

In this section, the lift, drag, and pitching moment coefficients of E387 and A7 obtained from the QMUL experiments are compared to show the improvements in the aerodynamic performance resulting from removing the gradient-of-curvature discontinuities at Reynolds numbers 1×10^5 , 2×10^5 , and 3×10^5 , as shown in Fig. 4.

A. Comparison with results from NASA LTPT

For validation purpose, the E387 results of the present experiments are compared with the NASA LTPT experimental data.¹⁵ The lift and pitching moment results from both QMUL and LTPT tests were obtained from surface pressure measurements, and the drag results were both

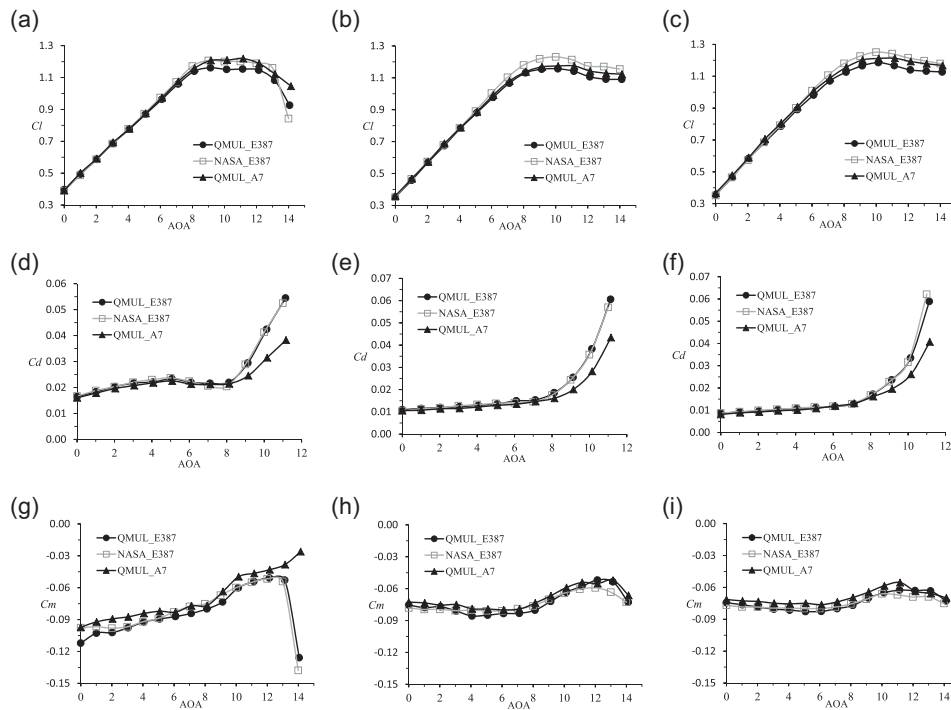


FIG. 4. Lift, drag, and pitching moment coefficients versus angles of attack obtained from both airfoils of current experiments and the airfoil E387 of the NASA LTPT experiments.¹⁵ (a), (b), (c), (d), (e), (f) and (g), (h), (i) are at Reynolds numbers 1×10^5 , 2×10^5 , and 3×10^5 , respectively.

obtained from the wake survey method. As shown in Fig. 4, the present experimental results generally show good agreement with the LTPT results. One of the discrepancies is in the lift results in the high angle of attack range at all three tested Reynolds numbers. The QMUL results of lift coefficients show lower values compared to the LTPT data in the angle of attack range from 9° to 14° .

One possible reason for the difference in the lift performance is that the number of surface pressure measurement positions in the present experiment is less than those in the LTPT experiment. This difference occurs mainly at the LE part because there was not enough space to fit more tubing in the current experiment. As mentioned earlier, all the copper pressure tubing was routed under the surface to keep the original designed surface curvature distributions of the airfoils to the maximum, while the LTPT machined grooves in the airfoil surface and routed all the tubing through the grooves and filled with epoxy resin. With the LTPT method, more pressure tubing can be used in the airfoil and hence more positions can be measured, but it is difficult to guarantee the surface curvature distribution of the original designed airfoil because curvature distributions are relatively sensitive to airfoil surface even if the appearance is very smooth.³¹ Since the emphasis of this paper is the effects of surface curvature, it is necessary to compromise between the quantity of surface pressure measurement positions and staying as close as possible to the original designed airfoil profile. The difference in the lift results at high angles of attack between QMUL and LTPT experiments does not affect the comparison between the results of E387 and A7 in the current tests, because the same number and positions of pressure tubing were used in each airfoil and same operating conditions were applied to both airfoils in the experiments. The E387 drag data obtained from the QMUL experiments show good agreement with the LTPT results. At the higher angles of attack, the current tests generally present slightly higher values of drag coefficients except 11° at $Re = 3 \times 10^5$. The differences in the drag coefficients can be attributed to the differences in turbulence intensity and surface curvature effects due to the reconstruction of the airfoil surface in the LTPT experiments.

B. Aerodynamic performance improvements

At all the three Reynolds numbers tested, the redesigned airfoil A7 with a continuous distribution of gradient-of-curvatures presented a lift increase and a drag decrease. At higher angles of attack, the airfoil A7 presents an obvious increase in lift coefficients and a remarkable decrease in drag coefficients, while at lower angles of attack it shows lower drag coefficients and similar lift coefficients. At 7° and 8° angles of attack, the two airfoils have equivalent aerodynamic performance. Here, $Re = 1 \times 10^5$ is selected as an example to analyze the reasons and mechanism for these improvements from the pressure coefficient distributions at typical angles of attack, as shown in Fig. 5.

At angles of attack of 0° and 4° , the airfoil A7 presents two main differences in the performance as compared to the airfoil E387. The removal of the gradient-of-curvature discontinuities results in (1) an increase in the pressure difference between the suction and pressure sides at the position between the LE and $x/c = 0.3$, and (2) a decrease in the pressure difference at the back part of the airfoil main body. The continuous distributions of gradient-of-curvature change the geometry of the nose part by up to 0.4% in the suction side and up to 0.14% in the pressure side based on the chord length, which makes the nose part up to 0.2% thicker based on the chord length. These slight profile changes directly increase the pressure difference between the suction and pressure sides by up to 13% near the nose part and thereby increases the lift coefficients. However, this does not result in an overall increase in lift because of the reduction offset of the pressure difference between the suction and pressure sides at the back part of the main body, at $x/c = 0.85$ in Fig. 5(a) and $x/c = 0.7$ in Fig. 5(b). The decrease in the pressure difference indicates that the turbulent re-attachment on the suction side of the airfoil A7 occurs earlier than the airfoil E387. While they have similar positions of the laminar separation, earlier turbulent re-attachments result in shorter laminar separation bubbles, leading to a decrease in the airfoil drag coefficients as shown in Fig. 4(b). Similar situations can be found in other low angles of attack.

With the increase in the angle of attack at the same Reynolds number, the laminar separation bubble moves towards the LE and decreases its bubble length. The effects of the surface curvature on reducing the bubble size thereupon become less obvious. In Fig. 5(c), E387 and A7 have similar pressure coefficients distributions and hence similar lift and drag coefficients at 7° . The designed angle of attack of E387 aiming for the maximum lift-to-drag ratio is approximately 7.5° and it makes sense that the airfoil E387 presents optimum performance at an angle of attack near the design angle. The continuous distributions of gradient-of-curvature provide equivalent aerodynamic performance at this attack angle.

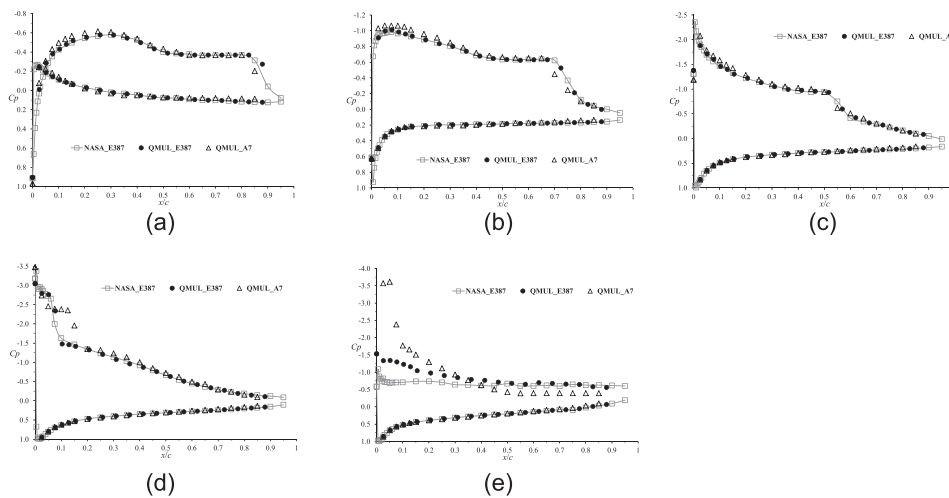


FIG. 5. Pressure coefficient distributions at typical angles of attack obtained from both airfoils of current experiments and the airfoil E387 of the NASA LTPT experiments.¹⁵ (a), (b), (c), (d), and (e) represent angles of attack of 0° , 4° , 7° , 10° , and 14° , respectively, at Reynolds number 1×10^5 .

At angles of attack of 10° , the airfoil A7 presents an increase in the pressure difference between the suction and pressure sides at the airfoil nose part as shown in Fig. 5(d). This indicates a larger size of laminar separation bubble compared to the airfoil E387. Horton³⁹ concluded that the growth and bursting behavior of laminar separation bubble in incompressible flow can be summarized in three stages. At a constant low Reynolds number, the bubble presents as a relatively long bubble on the airfoil suction side in the low angle of attack range (Stage 1), and it moves towards the LE region and reduces the bubble size with the increasing angle of attack. When the angle of attack increases to a moderate value (e.g., 10°), the bubble appears at the LE region as a “short bubble” (Stage 2). The bubble bursts at the maximum-lift angle of attack resulting in the LE stall (Stage 3). This explains the reason for the bubble size difference near the LE part in the current case indicated in Figure 5(d). The C_p results indicate that the gradient-of-curvature discontinuities make the bubble on E387 move into Stage 2 prematurely, while the bubble on the airfoil A7 with an improved curvature distribution is still in Stage 1. Generally, the drag force shows an increase from Stage 1 to Stage 2 due to the more energetic turbulent boundary layer, and a bursting increase from Stage 2 to Stage 3 due to the LE stall. Consequently, A7 has increased the magnitudes of C_l (due to the higher value of pressure difference between the suction and pressure sides of airfoil pressure and suction sides) and C_d performances (because the bubble is still at Stage 1), comparing to the premature laminar separation on the airfoil E387.

As presented in Fig. 5(e), the airfoil E387 experiences a sudden drop in C_p distributions at the angle of attack of 14° , while the airfoil A7 retains a normal distribution compared to the lower angles of attack. This phenomenon indicates that the separation bubble on the airfoil E387 burst, resulting in the LE stall (Stage 3 as mentioned previously). The airfoil A7 retains a “short bubble” at the LE region (Stage 2 as mentioned previously), which can also be confirmed by the pitching moment distribution as shown in Fig. 4(c). This accurately explains why the sudden drop in C_l distributions and the bursting increase in C_d distributions occur to the airfoil E387 but not to the airfoil A7 at 14° . Thus, the continuous distributions of gradient-of-curvature can increase the stalling angle of attack.

The airfoil performance at this Reynolds number is dominated by the laminar separation bubbles. It was presented that the airfoil with the continuous distributions of gradient-of-curvature has a better control on the bubble stage and hence better aerodynamic performance at the same low TI.

One might be interested in the effects of a higher TI on the airfoil performance. Studies show that a significant delay in the stall can be observed when the TI was raised to 4% or more,^{33–35} while Li *et al.*⁴⁰ argued that the increased TI may not delay the stall for all the Reynolds number as the stall phenomenon cannot be observed at a low TI and a very low Reynolds number. Meanwhile, literature results showed mixed views on the effects of higher TI on the lift performance and laminar separation bubbles (LSBs), especially when the angle of attack (AoA) is lower than the stalling AoA determined at a low TI. Literatures suggested that there are no significant changes in the lift-AoA curve below the low-TI stalling angle with a higher TI.^{33–35} Swalwell *et al.*³⁵ observed that the LSB region in pressure distributions of the aerofoil 4421 at 10° AoA barely change with four different TIs, indicating that a higher TI barely affects the size of the LSB. However, Stack⁴¹ reported that the maximum lift coefficients of NACA 0006 and NACA0021, as well as their lift coefficients before the low-TI stalling angle, decreased with a higher TI at low Reynolds numbers. Lower lift coefficients indicate that the size of the LSB decreased with an increasing TI, possibly resulting from a premature laminar-turbulence transition. Moreover, the oil flow visualization work of Hoffmann⁴² showed that the LSB disappeared on an NACA0015 airfoil at AoA of 17° and Reynolds number 2.5×10^5 when the TI was increased to 9%.

It is expected that the stalling angle of the aerofoil with slope-of-curvature discontinuities will be increased when increasing the turbulence intensity based on the literature,^{33–35} and removing the slope-of-curvature discontinuities from the aerofoil may further improve the aerodynamic performance including the stalling angle and the LSB size according to the current study. This is still open for future investigation.

C. The effects of Reynolds number

The effects of the surface curvature on the airfoils' performance vary with different angles of attack and Reynolds numbers. Fig. 6 illustrates the effects of Reynolds numbers on chordwise pressure distributions at 4° and 10° attack angles which represent lower and higher angles of attack, respectively. In Fig. 6(a), the pressure data indicate a shrinking of the laminar separation bubbles on both airfoils at Reynolds numbers from 100 000 to 300 000. The surface curvature effects on the bubble size reduction are consistent at all three Reynolds numbers at $AoA = 4^\circ$. Correspondingly, the reduced drag coefficient is essentially consistent at this angle of attack as indicated in Figs. 4(b), 4(e), and 4(h).

As analyzed in Subsection IV B, the improved curvature distributions delay the progress of the separation bubble towards the LE, so the separation bubble on A7 is in a different stage compared to E387, resulting in a better aerodynamic performance. However, this improvement becomes less significant with the increasing Reynolds numbers as illustrated in Fig. 6(b). Correspondingly, the difference of C_d between E387 and A7 decreases from more than 0.01 at $Re = 1 \times 10^5$ to less than 0.007 at $Re = 3 \times 10^5$ as shown in Fig. 4. Thus, a higher Reynolds number moderates the effects of surface curvature on the airfoil performance at higher angles of attack.

D. Comparison of results with RANS computations

In many circumstances, the results obtained from experiments are often unavailable because of the economic and temporal costs for providing different operating conditions and testing models. Hence, Computational Fluid Dynamics (CFD) is used widely in the field of wind energy.^{43,44} With proper experimental validations for the theoretical turbulent model, RANS computations can be an efficient alternative to experimental testing, in terms of prediction of airfoil aerodynamic and aeroacoustic performance^{45,46} and airfoil optimization for small wind turbines.^{9,47} RANS computations also provide the necessary supplements such as skin friction distributions and separation bubble visualizations to the experimental testing. In this section, RANS computations are applied to the airfoils E387 and A7 under the same experimental operating conditions. For both airfoils, 1200 nodes were distributed around the airfoil surface and a 30 chord-length computational domain which contains approximately 270 000 mesh cells was used after checking the mesh independence. Depending on different Reynolds numbers and angles of attack, at least 150 uniform nodes were distributed to the zone of laminar separation bubble to seize the bubble features, and $y^+ \leq 1.0$ were kept for all the cases. In terms of the eddy viscosity model, the RANS computations used the four equations transition Shear Stress Transport (SST) model in ANSYS Fluent 16.0. More mesh details are described in Ref. 30.

Fig. 7 presents a comparison between the lift-drag coefficients' polar curves obtained from the current experiments and RANS computations for the Reynolds number of 1×10^5 . Generally, a better agreement is found at angles of attack lower than 8° while the RANS computations overestimate the drag data at higher angles of attack. The lift prediction errors of

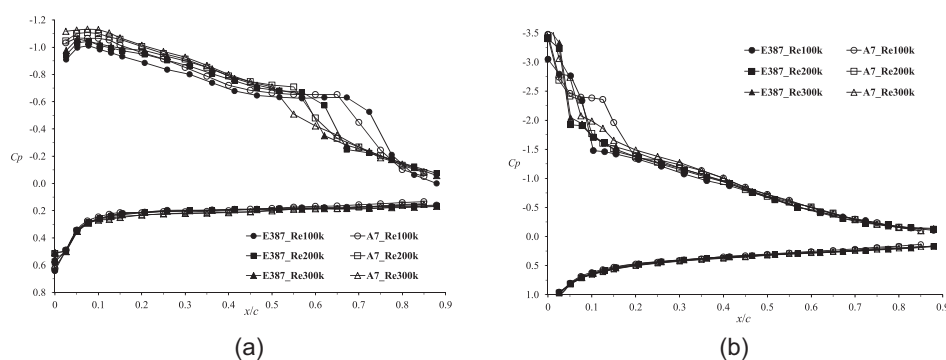


FIG. 6. Effect of Reynolds number on chordwise pressure distributions. (a) $AoA = 4^\circ$ and (b) $AoA = 10^\circ$.

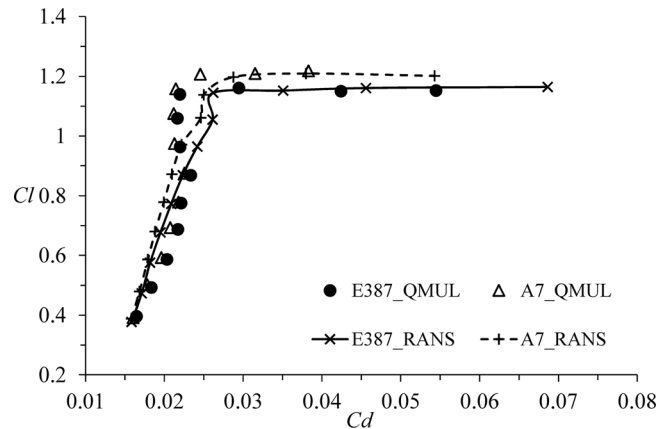


FIG. 7. Comparison of lift-drag coefficients polar curves between RANS results and present experimental work at Reynolds number 1×10^5 . The angles of attack of the experimental data range from 0° to 11° .

RANS are within 5%, and the drag prediction errors are generally within 10% except 10° and 11° attack angles, pointing to the sensitivity of drag computations at higher angles of attack.

Detailed data of 4° and 10° attack angles are selected as typical results, as shown in Figs. 8 and 9. The RANS results accurately predict the increase in the pressure difference near the airfoil nose part due to the improved curvature distributions in Fig. 8(a). The extent reduction of the laminar separation bubble due to an early turbulent re-attachment was predicted, although in both cases the RANS computations prematurely predict the re-attachment positions. The appearance and extent of the laminar separation bubbles on both airfoils obtained from the RANS computations are presented in Fig. 8(b). The computational results indicate that the continuous distributions of gradient-of-curvature reduce not only the bubble length but also the bubble height.

The size of the laminar separation bubble in Fig. 8(b) including lengths and areas is presented specifically in Table I. The bubble extents were bounded by the airfoil surface and the streamlines. The bubble boundary coordinates were integrated to obtain the bubble areas. The bubble length obtained from the NACA LTPT experiments¹⁵ is acceptably reproduced. The table indicates a 10.5% bubble length decrease and a 16.5% bubble area decrease due to the gradient-of-curvature continuity.

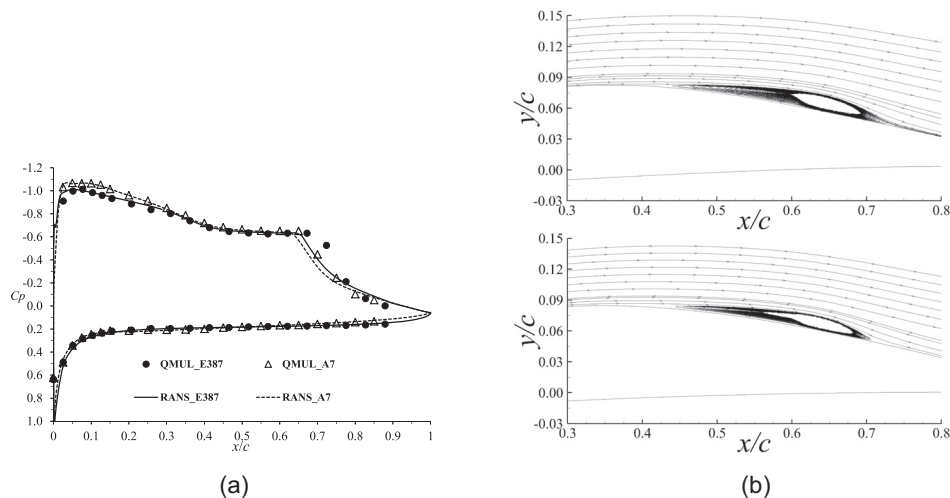


FIG. 8. Comparisons of (a) surface pressure coefficients between RANS computational results and current experiments (b) computational streamlines of laminar separation bubbles. Both comparisons are between the airfoil E387 and A7 at $AoA = 4^\circ$ for Reynolds number 1×10^5 .

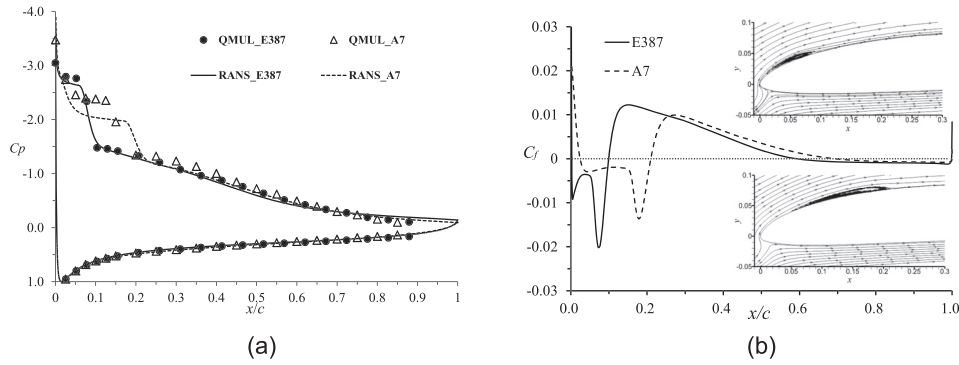


FIG. 9. RANS computational results of (a) pressure coefficients and (b) skin friction coefficients distributions of the airfoil E387 and A7 at $A\alpha A = 10^\circ$, Reynolds number 1×10^5 . The streamline figures in (b) are the streamline of E387 (top) and A7 (bottom) for the current Reynolds number and $A\alpha A$.

The reduction in bubble size is caused by the variation of the adverse pressure gradient due to the continuity of local surface gradient-of-curvature. In the current case, two critical positions, where curvature distributions are improved, are the nose part (from LE to $x/c = 0.3$ approximately) and the TE circle of the airfoil, resulting in an increase in the adverse pressure gradient and hence a decrease in the bubble size.

In Fig. 9(a), the RANS results offer an acceptable prediction, although on the suction side of the airfoil RANS cannot predict C_p accurately at the nose part. On the suction side, RANS computations also slightly underestimate C_p at the main body part and slightly overestimate C_p near the TE part. The length of the laminar separation bubble is well predicted and the streamlines are shown in Fig. 9(b). The RANS results are in accordance with Horton's theory³⁹ as the separation bubbles are in different stages due to the differences of gradient-of-curvature continuities.

The skin friction coefficients predictions in Fig. 9(b) show at $Re = 1 \times 10^5$ and $A\alpha A = 10^\circ$, the continuous distributions of gradient-of-curvature delayed the position of turbulence TE separation by more than 10% for the redesigned airfoil A7. As soon as the flow separates near the TE, the separated region merges with the wake and results in the TE stall, causing lift loss and drag increase. The continuous distributions of gradient-of-curvature make the boundary layer flow attach to the airfoil surface for a longer surface distance and suppress the flow separation in the TE, and consequently improve the airfoil performance.

V. ESTIMATION OF THE IMPROVEMENT TO POWER GENERATION

In this section, we select a 3 kW small wind turbine blade to demonstrate the improvement in output energy resulting from replacing its airfoil E387 with A7 while all other parameters of the wind turbine are unchanged. The wind turbine parameters are presented in Table II and the chord length distribution of the blade is presented in Fig. 10.

The steady Blade Elements Momentum (BEM) method based on the work of Wilson and Lissaman⁴⁸ is used to calculate the power coefficient curve and the power curve on 26 blade sections, as presented in Fig. 11. All the aerodynamic parameters including lift and drag coefficients of the blade sections (airfoils) are interpolated from the experimental results of this

TABLE I. The laminar separation bubble extent from the RANS simulations and the LTPT experiments¹⁵ at $A\alpha A = 4^\circ$ for Reynolds number 1×10^5 . The bubble length and area are normalized by the chord length and the square of the chord length, respectively.

Bubble length	Bubble area			
	E387	A7	E387	A7
E387_LTPT				
0.38	0.359	0.321	0.00297	0.00248

TABLE II. Parameters of a small wind turbine using the airfoil E387.

Rated power (kW)	Blade length (m)	Rated rotating speed (rpm)	Rated wind speed (m/s)	Cut-in speed (m/s)	Cut-out speed (m/s)
3.0	1.85	250	10.5	4	15

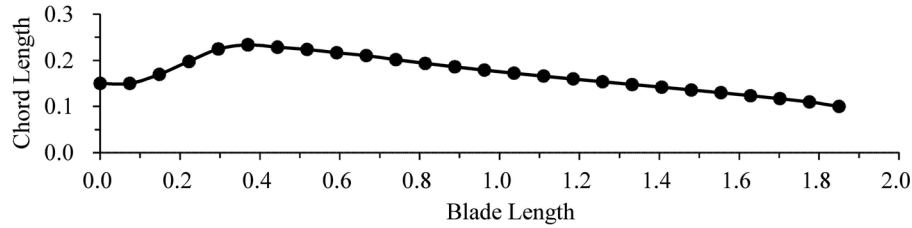


FIG. 10. Chord length distribution of the blade of the small wind turbine.

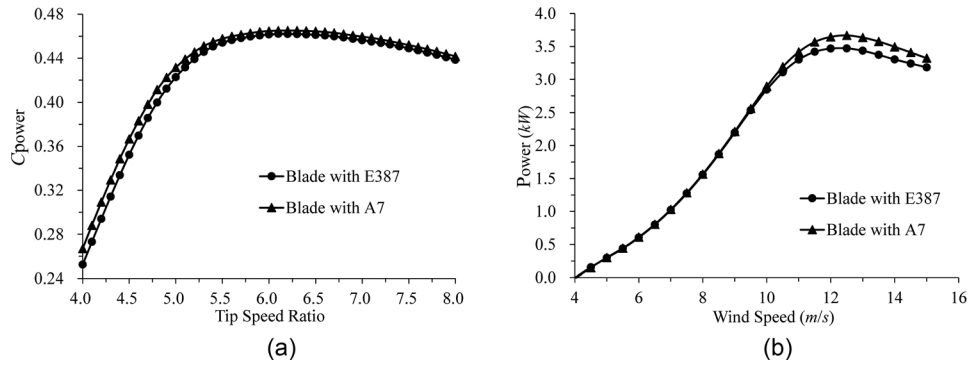


FIG. 11. Comparison of (a) power coefficients curve and (b) power curve of the blade with the airfoil E387 and A7.

study. The force coefficients were extrapolated to 360° using NREL's AirfoilPrep⁴⁹ based on Viterna's method.⁵⁰ The Wilson's thrust coefficient formula⁵¹ is used for large induced velocity states. The Prandtl's tip-loss function⁵² was applied to the blade tip as well as the root.

Fig. 11(a) shows that the blade made with the airfoil A7 presents higher power coefficients at all tip speed ratios (TSRs). A 6% power coefficient increase is obtained at TSR 4.5 when replacing the airfoil E387 with A7 for the small wind turbine. The blade made with the airfoil A7 reaches a slightly higher maximum power coefficient 0.465 at TSR 6. The power curve in Fig. 11(b) presents an obvious increase when the wind speed reaches rated speed. The increase is up to 10% at wind speed 12.5 m/s.

Annual energy production (AEP) is also calculated in Table III to estimate the overall improvement to power generation. Here, the AEP means the energy production in theory, which does not consider uncertainty elements including air density reduction, control misalignment, fault and wakes loss. The Weibull distribution⁵³ (Weibull parameter $k=2$, corresponding average wind speed 5 m/s) is used to represent the wind speed frequency distribution. Table III illustrates that the AEP of small wind turbines can be increased by 1.62% by simply replacing

TABLE III. Annual energy production of the wind turbine estimated with the airfoils E387 and A7.

	With E387	With A7	Increasing AEP	Increasing ratio
AEP (kW h)	5222.56	5307.26	84.7	1.62%

with the airfoils with the continuous curvature and gradient-of-curvature distributions. Considering the cumulative installed capacity of small wind turbines, the increasing percentage of the AEP is considerably remarkable.

VI. CONCLUDING REMARKS

The surface gradient-of-curvature discontinuities in the airfoil E387 were removed using the CIRCLE method. The newly designed airfoil A7 slightly deviates in its profile geometry from the original airfoil but it has a continuous distribution of gradient-of-curvature. The wind tunnel experiments were conducted by both airfoils at low Reynolds numbers, and RANS computations under the same operating conditions were used as a supplement and comparison to the experiments.

The effects of the gradient-of-curvature distribution on the airfoil performance are more profound at higher angles of attack and lower Reynolds number. For low Reynolds numbers, the airfoil performance is dominated by laminar separation bubbles. The separation bubble sizes were deduced from the experimental results of C_p distributions and visualized by the RANS results which compared well against the available experimental data in the literature. For the cases at low angles of attack, the continuity of surface gradient-of-curvature affects the pressure difference between the suction and pressure sides of the airfoil. The continuous distribution of gradient-of-curvature significantly reduced the bubble sizes and hence the drag coefficients. At higher angles of attack, the continuous distribution of gradient-of-curvature delayed LE separation, laminar-turbulence transition, and TE separation, resulting in an improved lift and drag performance. Through these mechanisms, the airfoil A7 achieved a higher stalling angle. The continuous curvature and distributions of gradient-of-curvature result in a better control of the laminar separation bubbles and flow separation to reduce drag, and better airfoil profile increasing the pressure difference between the suction and pressure sides to increase lift.

A 3 kW small wind turbine was used to estimate the output energy improvement by replacing its original airfoil E387 with the airfoil A7. Based on the ideal situations, the increment of the estimated output power is up to 10% and the increment of the annual energy production is 1.62% which is considerably remarkable based on the cumulative installed capacity of small wind turbines. The continuous distributions of gradient-of-curvature resulted in higher aerodynamic and energy efficiency.

It has been experimentally and numerically shown that the distribution of surface gradient-of-curvature has significant effects on the low Reynolds number airfoil performance by affecting the boundary layer behavior. The research provides an aerodynamic method to increase the power generation efficiency of small wind turbines through improving the airfoil performance, without changing the airfoil profile significantly or importing other devices.

ACKNOWLEDGMENTS

The authors acknowledge Mr. Jianghai Wu for providing the 3 kW small wind turbine information and Dr. F. Motallebi for his assistance with hot wire calibration. Ph.D. students and postdocs, who over the past two decades have contributed to coding various aspects of the CIRCLE blade design method in FORTRAN, C and MATLAB are also acknowledged. The Ph.D. research of Xiang Shen was funded by China Scholarship Council (CSC)/Queen Mary Joint Ph.D. scholarship.

¹World Wind Energy Association, Small Wind World Report No. 2014, Bonn, Germany, March, 2014.

²T. Korakianitis, M. A. Rezaenia, X. Shen, E. J. Avital, A. Munjiza, P. H. Wen, and J. Williams, "Aerodynamics of wind turbine technology," in Handbook of Clean Energy Systems (Wiley, 2015).

³T. G. Wang, L. Wang, W. Zhong, B. F. Xu, and L. Chen, "Large-scale wind turbine blade design and aerodynamic analysis," *Chin. Sci. Bull.* **57**(5), 466–472 (2012).

⁴Y. Li, "The status of large scale wind turbine technology development," *Appl. Math. Mech.* **34**(10), 1003–1011 (2013).

⁵N. D. Sandham, "Transitional separation bubbles and unsteady aspects of aerofoil stall," *Aeronaut. J.* **112**(1133), 395–404 (2008).

⁶R. K. Singh and M. R. Ahmed, "Blade design and performance testing of a small wind turbine rotor for low wind speed applications," *Renewable Energy* **50**, 812–819 (2013).

- ⁷K. W. Van Treuren, "Small-scale wind turbine testing in wind tunnels under low Reynolds number conditions," *J. Energy Resour. Technol.* **137**(5), 051208 (2015).
- ⁸P. Giguere and M. S. Selig, "New airfoils for small horizontal axis wind turbines," *J. Sol. Energy Eng.* **120**(2), 108–114 (1998).
- ⁹K. R. Ram, S. Lal, and M. R. Ahmed, "Low Reynolds number airfoil optimization for wind turbine applications using genetic algorithm," *J. Renewable Sustainable Energy* **5**(5), 052007 (2013).
- ¹⁰D. M. Somers and M. D. Maughmer, "Theoretical aerodynamic analyses of six airfoils for use on small wind turbines," Technical Report No. NREL/SR-500-33295, National Renewable Energy Laboratory, 2003.
- ¹¹J. C. C. Henriques, F. Marques da Silva, A. I. Estanqueiro, and L. M. C. Gato, "Design of a new urban wind turbine airfoil using a pressure-load inverse method," *Renewable Energy* **34**(12), 2728–2734 (2009).
- ¹²M. Islam, M. R. Amin, D. S.-K. Ting, and A. Fartaj, "Selection of airfoils for straight-bladed vertical axis wind turbines based on desirable aerodynamic characteristics," in *ASME 2008 International Mechanical Engineering Congress and Exposition* (American Society of Mechanical Engineers, 2008), pp. 3–12.
- ¹³M. Marnett, S. Yang, and W. Schroder, "Lightweight airfoil design for a series of small vertical axis wind turbines," in *European Wind Energy Conference and Exhibition* (2010), Vol. 6, pp. 4232–4238.
- ¹⁴R. K. Singh, M. R. Ahmed, M. A. Zullah, and Y.-H. Lee, "Design of a low Reynolds number airfoil for small horizontal axis wind turbines," *Renewable Energy* **42**, 66–76 (2012).
- ¹⁵R. Mcghee, B. Walker, and B. Millard, "Experimental results for the Eppler 387 airfoil at low Reynolds numbers in the Langley low-turbulence pressure tunnel," NASA Technical Memorandum 4062, NASA, 1988.
- ¹⁶M. S. Selig, R. W. Deters, and G. A. Williamson, "Wind tunnel testing airfoils at low Reynolds numbers," in *49th AIAA Aerospace Sciences Meeting* (2011), pp. 4–7.
- ¹⁷I. A. Hamakhan and T. Korakianitis, "Aerodynamic performance effects of leading-edge geometry in gas-turbine blades," *Appl. Energy* **87**(5), 1591–1601 (2010).
- ¹⁸K. Siddappaji, M. G. Turner, and A. Merchant, "General capability of parametric 3D blade design tool for turbomachinery," in *ASME Turbo Expo 2012: Turbine Technical Conference and Exposition* (American Society of Mechanical Engineers, 2012), pp. 2331–2344.
- ¹⁹T. Korakianitis, "Design of airfoils and cascades of airfoils," *AIAA J.* **27**(4), 455–461 (1989).
- ²⁰A. F. Nemem, M. G. Turner, K. Siddappaji, and M. Galbraith, "A smooth curvature-defined meanline section option for a general turbomachinery geometry generator," in *ASME Turbo Expo 2014: Turbine Technical Conference and Exposition* (American Society of Mechanical Engineers, 2014), p. V02BT39A026.
- ²¹H. P. Hodson, "Boundary-layer transition and separation near the leading edge of a high-speed turbine blade," *J. Eng. Gas Turbines Power* **107**(1), 127–134 (1985).
- ²²P. Stow, *Blading Design for Multi-Stage HP Compressors, Blading Design for Axial Turbomachines*, 1989.
- ²³T. Korakianitis, "Prescribed-curvature distribution airfoils for the preliminary geometric design of axial turbomachinery cascades," *Trans. ASME J. Turbomach.* **115**(2), 325–333 (1993).
- ²⁴A. P. S. Wheeler and R. J. Miller, "Compressor wake/leading-edge interactions at off design incidences," in *ASME Turbo Expo 2008: Power for Land, Sea, and Air* (American Society of Mechanical Engineers, 2008), pp. 1795–1806.
- ²⁵A. P. S. Wheeler, A. Sofia, and R. J. Miller, "The effect of leading-edge geometry on wake interactions in compressors," *J. Turbomach.* **131**(4), 041013 (2009).
- ²⁶A. Massardo, A. Satta, and M. Marini, "Axial flow compressor design optimization: Part II Throughflow analysis," *J. Turbomach.* **112**(3), 405–410 (1990).
- ²⁷A. F. Massardo and M. Scialo, "Thermoeconomic analysis of gas turbine based cycles," *J. Eng. Gas Turbines Power* **122**(4), 664–671 (2000).
- ²⁸T. Korakianitis, M. A. Rezaenia, I. A. Hamakhan, E. J. Avital, and J. J. R. Williams, "Aerodynamic improvements of wind-turbine airfoil geometries with the prescribed surface curvature distribution blade design (CIRCLE) method," *J. Eng. Gas Turbines Power* **134**(8), 082601 (2012).
- ²⁹Y. Song, C. W. Gu, and Y. B. Xiao, "Numerical and theoretical investigations concerning the continuous-surface-curvature effect in compressor blades," *Energies* **7**(12), 8150–8177 (2014).
- ³⁰X. Shen, T. Korakianitis, and E. J. Avital, "Numerical investigation of surface curvature effects on aerofoil aerodynamic performance," *Appl. Mech. Mater.* **798**, 589–595 (2015).
- ³¹T. Korakianitis, M. A. Rezaenia, I. A. Hamakhan, and A. P. S. Wheeler, "Two- and three-dimensional prescribed surface curvature distribution blade design (CIRCLE) method for the design of high efficiency turbines, compressors, and isolated airfoils," *J. Turbomach.* **135**(3), 041002 (2013).
- ³²A. Scupi, E. J. Avital, D. Dinu, J. J. R. Williams, and A. Munjiza, "Large eddy simulation of flows around a kite used as an auxiliary propulsion system," *J. Fluids Eng.* **137**(10), 101301 (2015).
- ³³X. Amandolese and E. Szechenyi, "Experimental study of the effect of turbulence on a section model blade oscillating in stall," *Wind Energy* **7**(4), 267–282 (2004).
- ³⁴K. E. Swalwell, J. Sheridan, and W. H. Melbourne *et al.*, "The effect of turbulence intensity on stall of the NACA 0021 aerofoil," in *14th Australasian Fluid Mechanics Conference* (2001), pp. 10–14.
- ³⁵K. E. Swalwell, J. Sheridan, and W. H. Melbourne, "The effect of turbulence intensity on performance of a naca4421 airfoil section," in *42nd AIAA Aerospace Sciences Meeting and Exhibit, Reno, Nevada. AIAA* (AIAA, 2004).
- ³⁶R. Shelquist, An introduction to air density and density altitude calculations, Internet Survey, 2012.
- ³⁷T. W. Schlatter and D. V. Baker, "Algorithms for thermodynamic calculations," in *NOAA/ERL PROFS Program Office, Boulder, CO* (1981), p. 34.
- ³⁸J. B. Barlow, A. Pope, and W. H. Rae, *Low Speed Wind Tunnel Testing*, 3rd ed. (Wiley, Chichester, New York), 1999.
- ³⁹H. P. Horton, "Laminar separation bubbles in two and three dimensional incompressible flow," PhD thesis, Queen Mary College, University of London, 1968.
- ⁴⁰S.-w. Li, S. Wang, J.-p. Wang, and J.-c. Mi, "Effect of turbulence intensity on airfoil flow: Numerical simulations and experimental measurements," *Appl. Math. Mech.* **32**, 1029–1038 (2011).
- ⁴¹J. Stack, "Tests in the variable density wind tunnel to investigate the effects of scale and turbulence on airfoil characteristics," Technical Report Technical Note 364, NACA, 1931.

- ⁴²J. A. Hoffmann, "Effects of freestream turbulence on the performance characteristics of an airfoil," *AIAA J.* **29**(9), 1353–1354 (1991).
- ⁴³M. J. Churchfield, Y. Li, and P. J. Moriarty, "A large-eddy simulation study of wake propagation and power production in an array of tidal-current turbines," *Philos. Trans. R. Soc. Lond., A* **371**(1985), 20120421 (2013).
- ⁴⁴E. Macheaux, G. C. Larsen, N. Troldborg, K. Hansen, N. Angelou, T. Mikkelsen, J. Mann *et al.*, "Investigation of wake interaction using full-scale lidar measurements and large eddy simulation," *Wind Energy* **19**(8), 1535–1551 (2016).
- ⁴⁵B. Hwang, T. Kim, S. Lee, and S. Lee, "Aeroacoustic analysis of a wind turbine airfoil and blade on icing state condition," *J. Renewable Sustainable Energy* **6**(4), 042003 (2014).
- ⁴⁶H. Y. Xu, S. L. Xing, and Z. Y. Ye, "Numerical study of the s809 airfoil aerodynamic performance using a co-flow jet active control concept," *J. Renewable Sustainable Energy* **7**(2), 023131 (2015).
- ⁴⁷S. Sanaye and A. Hassanzadeh, "Multi-objective optimization of airfoil shape for efficiency improvement and noise reduction in small wind turbines," *J. Renewable Sustainable Energy* **6**(5), 053105 (2014).
- ⁴⁸R. E. Wilson and P. B. S. Lissaman, "Applied aerodynamics of wind power machines," Technical Report No. PB-238595, Oregon State University, Corvallis, USA, 1974.
- ⁴⁹S. A. Ning, *AirfoilPrep.py* Documentation, Technical Report No. NREL/TP-5000-58817, National Renewable Energy Laboratory, 2013.
- ⁵⁰L. A. Viterna and D. C. Janetzke, "Theoretical and experimental power from large horizontal-axis wind turbines," Technical Report NASA TM-82944, National Aeronautics and Space Administration, 1982.
- ⁵¹R. E. Wilson, "Aerodynamic potpourri," in *Wind Turbine Dynamics* (NASA, 1981); abstract available at <http://adsabs.harvard.edu/abs/1981wtd..nasa....3W>.
- ⁵²T. Burton, D. Sharpe, N. Jenkins, and E. Bossanyi, *Wind Energy Handbook* (John Wiley & Sons, 2001).
- ⁵³J. V. Seguro and T. W. Lambert, "Modern estimation of the parameters of the Weibull wind speed distribution for wind energy analysis," *J. Wind Eng. Ind. Aerodyn.* **85**(1), 75–84 (2000).